SUPPLEMENATRY INFORMATION

Optical field-induced mass transfer in plasmonic electrochemistry

Johann V. Hemmer,[†] Md. Al-Amin,[†] and Andrew J. Wilson*

Department of Chemistry, University of Louisville, Louisville, Kentucky, 40292, United States

[†]Authors contributed equally to this work

*Corresponding author's e-mail: aj.wilson@louisville.edu

METHODS AND MATERIALS

The materials and methods used in this study have been previously reported.[S1,S2]

FINITE-ELEMENT SIMULATIONS

Light scattering on a Au nanoparticle

COMSOL's Wave Optics module was used to simulate the 3-dimensional electric field around a Au nanosphere of radius r_0 = 100 nm (approximation of average size of Au nanoscale features following electrochemical roughening, Figures S1 and S2) under laser illumination, using the scattered-field formulation:

$$\mathbf{E} = \mathbf{E}_b + \mathbf{E}_s \tag{1}$$

where $\mathbf{E}_b$ and $\mathbf{E}_s$ represent the background and scattered electric fields, respectively. COMSOL solves the frequency-domain governing equation

$$\nabla \times \mu_{\mathrm{r}}^{-1}(\nabla \times \mathbf{E}) - k_0^2\left(\varepsilon_{\mathrm{r}} - \frac{j\sigma}{\omega\varepsilon_0}\right)\mathbf{E} = 0 \tag{2}$$

in which μ_{r} and ε_{r} are the relative permeability and permittivity of the material, k_0 and ε_0 are the vacuum wavenumber and permittivity, respectively, σ is the material conductivity and ω is the angular frequency. The circularly polarized incident laser light is input as the background electric field, $\mathbf{E}_b$, as follows:

$$\mathbf{E}_b = \frac{E_0}{\sqrt{2}}(\hat{\mathbf{x}} + j\hat{\mathbf{y}})e^{-jkz} \tag{3}$$

The incident electric field amplitude, E_0, is calculated from the intensity of the incident light, I_0, measured experimentally, using the relationship

$$I = \frac{cn\varepsilon_0}{2}E^2 \tag{4}$$

where c is the speed of light in vacuum and n is the refractive index of the medium.

The geometry and 3D mesh of the system is presented in Figure S3. The Au nanoparticle is located at the origin of the model. A layer of water extends half a wavelength away from the nanoparticle surface and represents the far-field domain, followed by a perfectly matched layer of the same thickness. As indicated by Equation 3, the wave propagates along the z axis. Au and H_2O's complex $\varepsilon_{\mathrm{r}}(\omega)$ were obtained from Rakić *et al.*[S3] and Daimon and Masumura,[S4] respectively.

Figure S1. Representative images of an electrochemically roughened Au electrode obtained from scanning electron microscopy. Each panel indicates a different region of the electrode surface. The scale bar applies to all panels.

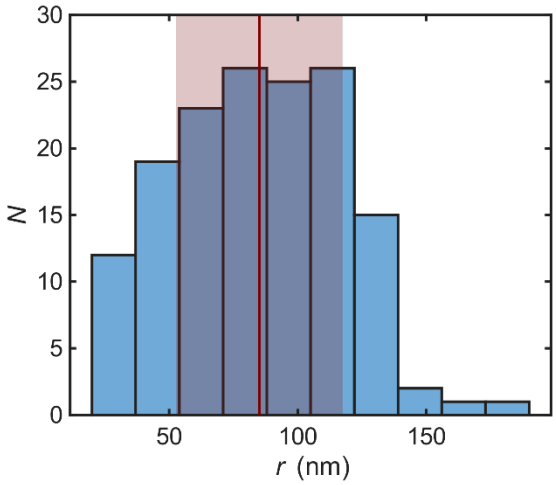

Figure S2. Histogram of the radius of nanostructures obtained from the SEM images in Figure S1, showing the average value and the 1*s* area.

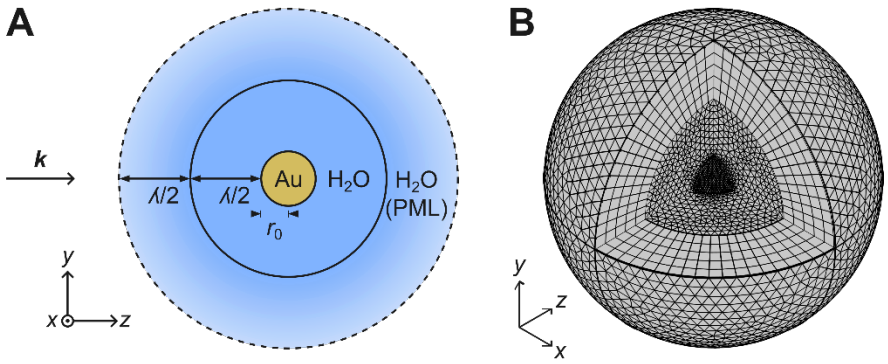

Figure S3. (A) Diagram and (B) computed finite-element mesh of the water-Au nanoparticle system used in simulations of electric near-fields.

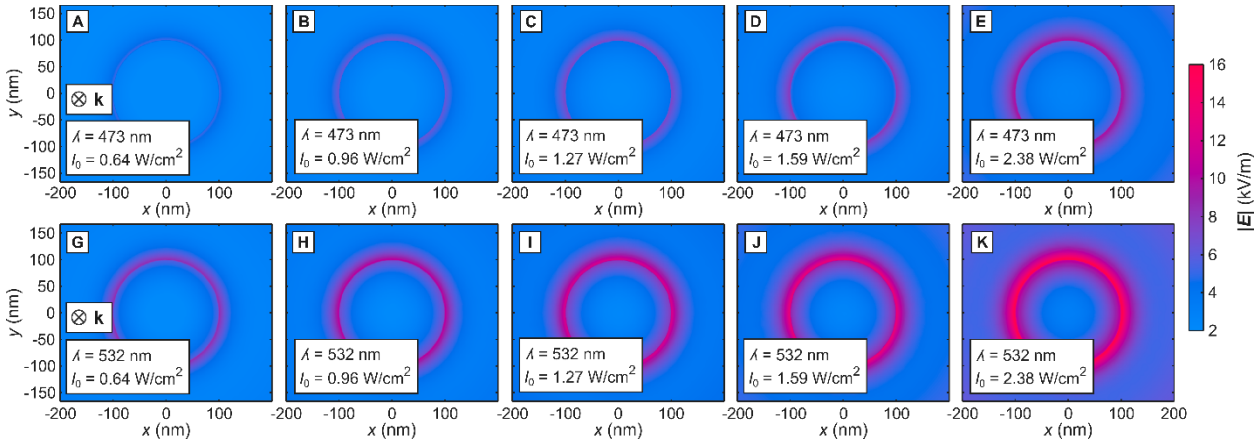

Figure S4. Simulated cross-sections of the electric field magnitude, |**E**|, around a Au nanoparticle in water when illuminated by circularly polarized light at different intensities I_0 and wavelengths λ. Direction of light propagation is indicated by the wave vector **k**. Top panels (A–E) correspond to λ = 473 nm and bottom panels (G–K) to λ = 532 nm. Intensity increases from left to right, from 0.64 to 2.38 W cm^{-2}.

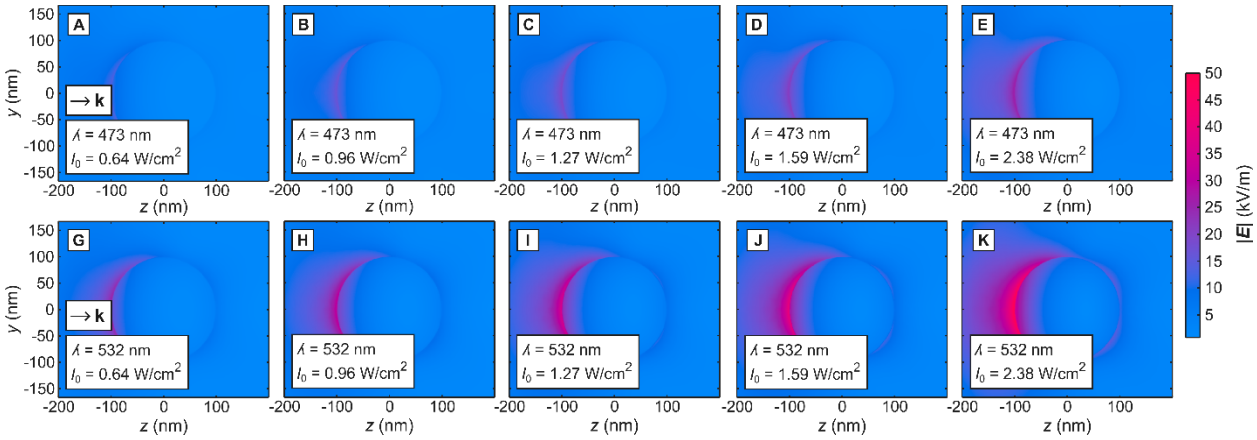

Figure S5. Simulated cross-sections of the electric field magnitude, |**E**|, around a Au nanoparticle in water when illuminated by circularly polarized light at different intensities I_0 and wavelengths λ. Direction of light propagation is indicated by the wave vector **k**. Top panels (A–E) correspond to λ = 473 nm and bottom panels (G–K) to λ = 532 nm. Intensity increases from left to right, from 0.64 to 2.38 W cm^{-2}. Panels E and K are reproduced from Figure 1A and 1B, respectively.

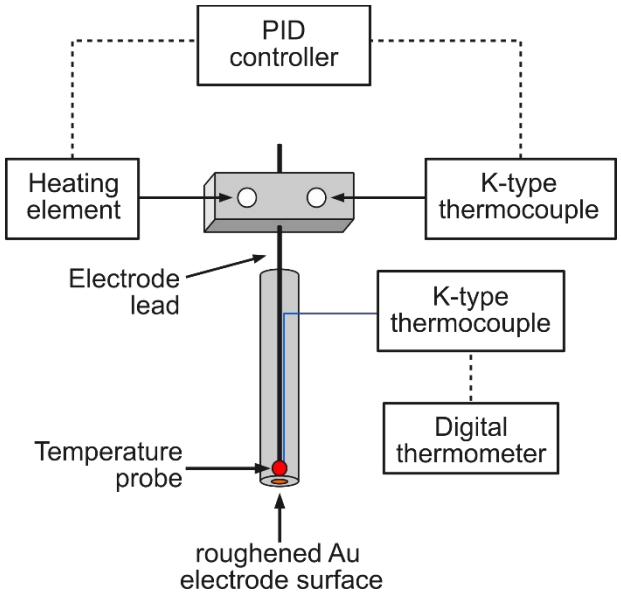

Figure S6. Schematic of heated electrode assembly. A closed-loop system maintains the temperature of the aluminum block, controlled using a resistive heating element, and a K-type thermocouple for feedback via a PID controller. A second K-type thermocouple, inserted into the electrode sheath, measures the temperature near the working electrode surface and outputs it to a digital thermometer.

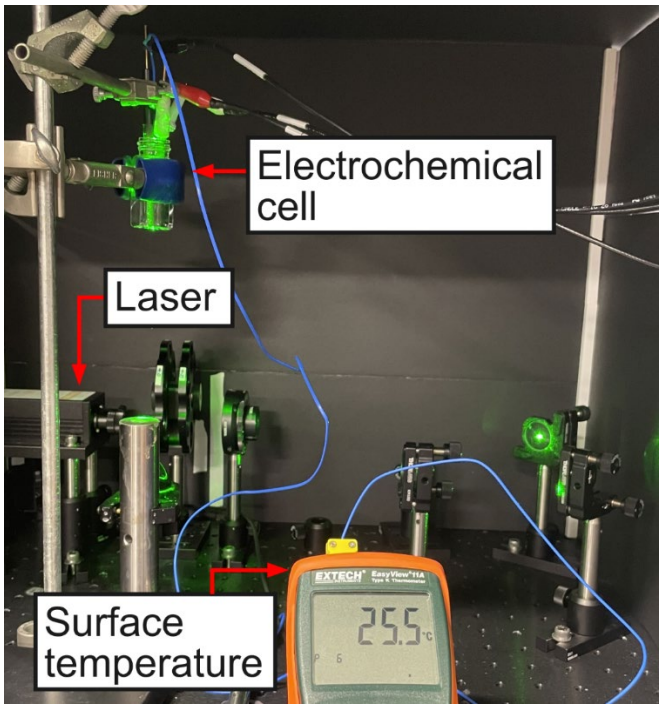

Figure S7. Photograph of the experimental setup showing the electrochemical cell, laser setup, and digital thermometer connected to the thermocouple used to measure the temperature near the surface of the working electrode.

Table S1. Electrode surface temperatures measured under different intensities at 532 nm illumination.

	T_{surf} (°C) as a function of I_0 (W cm^{-2}) at 532 nm					
Trial / I_0	**0.00**	**0.64**	**0.96**	**1.27**	**1.59**	**2.38**
1	22.7	23.2	23.5	23.7	24.1	25.6
2	22.1	22.7	23.0	23.3	23.7	25.5
3	23.4	23.8	24.0	24.2	24.4	25.5
Average	22.7	23.2	23.5	23.7	24.1	25.5
Std. dev.	0.7	0.6	0.5	0.5	0.4	0.1

Table S2. Electrode surface temperatures measured under different intensities at 473 nm illumination.

	T_{surf} (°C) as a function of I_0 (W cm^{-2}) at 473 nm					
Trial / I_0	**0.00**	**0.64**	**0.96**	**1.27**	**1.59**	**2.38**
1	21.9	24.5	25.5	26.5	27.5	29.4
2	23.1	24.5	25.6	26.4	27.4	29.2
3	23.7	24.6	24.5	26.5	27.5	29.7
Average	22.9	24.5	25.2	26.4	27.4	29.5
Std. dev.	1.0	0.0	0.6	0.1	0.1	0.3

Mass transfer in electrolyte

Finite-element simulations of the mass transfer in the electrochemical cell were performed based on our previous work.[S1,S2] For the Laminar Flow module, the Navier-Stokes equations are solved for the velocity field **u** of the electrolyte. Assuming a steady-state system and for weakly compressible flow, the continuity equation (5) is:

$$\nabla \cdot (\rho \mathbf{u}) = 0 \tag{5}$$

And the momentum equation (6) is

$$\rho(\mathbf{u} \cdot \nabla)\mathbf{u} = \nabla \cdot \left[-pI + \mu(\nabla \mathbf{u} + (\nabla \mathbf{u})^{\mathrm{T}}) - \frac{2}{3}\mu(\nabla \cdot \mathbf{u})I\right] + (\rho - \rho_{\mathrm{ref}})\mathbf{g} \tag{6}$$

where ρ is the density of the fluid, p is the pressure, μ is the dynamic viscosity, and **g** is the acceleration due to gravity. The initial velocity field **u** is assumed to be zero, simulating an initially quiescent solution. The driving force for convection is a change in ρ, which is caused by temperature gradients across the fluid. Thus, the temperature distribution must be calculated using the Heat Transfer in Fluids module. The Laminar Flow and Heat Transfer in Fluids modules are interfaced with the Nonisothermal Flow Multiphysics, which is calculated assuming a steady-state system. The temperature of each element is determined by solving the heat balance expressed by Equation 7,

$$\rho C_p \mathbf{u} \cdot \nabla T + \nabla \cdot \mathbf{q} = Q_p + Q_{\mathrm{vd}} + Q \tag{7}$$

where C_p is the specific heat capacity of the fluid at constant pressure, **q** is the heat flux due to conduction, Q_p is work done by pressure changes, Q_{vd} is heat by viscous dissipation and Q represents any other heat sources. The electrode assembly was assumed to be thermally insulated. Therefore, heat transfer would occur from the electrode surface to the solution, and between the solution and the surrounding ambient air. When solving equation (3), Q_p and Q_{vd} were neglected since the temperature range is small and viscous dissipation is low in the laminar regime. It is assumed that there is no mass transfer at the outer bounds of the electrolyte (where the glass walls of the vial are), but Q is assumed to be the convective heat flux between the electrolyte and the ambient air through the cell walls and the air-liquid interface. This heat flux is given by

$$Q = h_{\mathrm{air}}(T - T_{\mathrm{air}}) \tag{8}$$

where h_{air} is the convective heat transfer coefficient of air, estimated to be 20 W m^{-2} K^{-1}. At the electrode surface ($z = 0$, $0 \geq r \geq r_{\mathrm{e}}$), the temperature is input as T_{surf} from experimental data.

For the electrochemical simulations, COMSOL's Electroanalysis module was used, assuming a redox reaction in the form

$$\mathrm{O} + e \rightleftharpoons \mathrm{R} \tag{9}$$

to represent the Ru(III) and Ru(II) hexamine redox couple. The reaction is modeled assuming Butler-Volmer kinetics. The local current density at the electrode surface is calculated as a function of the overpotential:

$$j = j_0\left[e^{\alpha n f \eta} - e^{-(1-\alpha) n f \eta}\right] \tag{10}$$

In the equation, $f = F/RT$, $\eta = E - E_{\mathrm{eq}}$ and $E = \phi_s - \phi_l$. F and R are Faraday's constant and the universal gas constant, respectively. T is the temperature. E is the electrode potential, E_{eq} is the equilibrium potential, ϕ_s and ϕ_l are the electric potentials of the electrode and electrolyte, respectively. The exchange current density, j_0, is calculated using the mass action law assuming a reference exchange current density value, $j_{0,\mathrm{ref}}$, estimated through

$$j_{0,\mathrm{ref}} = k^0 F c_{\mathrm{ref}} \tag{11}$$

where k^0 is the heterogeneous electron transfer rate constant (determined experimentally to be 0.021 cm/s)[S1] and c_{ref} is the reference concentration (≡ 1 M). The electrode potential E is the applied potential during the chronoamperometry experiment (−0.45 V vs. Ag/AgCl), while E_{eq} is defined by the Nernst equation (activity coefficients assumed to be 1)

$$E_{\mathrm{eq}} = E_{\mathrm{eq}}^0 - \frac{1}{nf} \ln \frac{c_{\mathrm{R,s}}}{c_{\mathrm{O,s}}} \tag{12}$$

where E_{eq}^0 is the standard reduction potential of the redox couple (approximated experimentally as $E_{1/2}$ = 0.037 V vs. Ag/AgCl)[S1], and $c_{\mathrm{R,s}}$ and $c_{\mathrm{O,s}}$ are the concentrations of R and O at the electrode surface, respectively. The initial concentrations of the redox species (c_{O} and c_{R}) are assumed to be the same used in the experiments (5 and 0 mM, respectively). The transport of O and R in the electrolyte was calculated using the time-dependent Nernst-Plank equation

$$\frac{\partial c_i}{\partial t} = \nabla \cdot \left[(D_i \nabla c_i) + z_i \mathbf{u}_{\mathrm{m},i} F c_i \nabla \phi_l - \mathbf{u} c_i \right] + R_i \tag{13}$$

where D_i is the diffusion coefficient of species i (assumed to be 0.5×10^{-5} cm^2/s for both species based on experimental data)[S1], z_i is the charge of species i, $\mathbf{u}$ is the velocity field of the fluid, and R_i represents the reaction rate of species i, which is a function of the current density j. The velocity field $\mathbf{u}$ determines the flow of the bulk fluid which, in turn, is governed by Equations 1 and 2. When simulating migration, the velocity of the fluid at the electrode surface was assumed to be $\mathbf{u}_{\mathrm{surf}}$, with only a z component towards the electrode surface.

The system was reduced to two concentric cylinders. The inner cylinder being the working electrode, and the outer being the electrolyte volume. Since that configuration contains radial symmetry, this allowed the system to be modeled as a 2D axisymmetric plane. The model was further simplified by simulating only half of the plane (Figure S9). After a full revolution about the r axis, a 3D model is created. The parameters shown in the diagram are shown in Table S3.

Heat transfer in solids

For the simulations involving the different directions of heat flux, the Heat Transfer in Solids and Liquids interface was used in COMSOL. The standard materials library was used to obtain the necessary properties for the Au electrode and the Cu wire of the electrode lead. Teflon was used as a surrogate for Kel-F, the material used as the electrode sheath. A point probe was used to measure the temperature where the thermocouple is situated in the real electrode assembly, approximately 1 mm above the electrode surface. The Global ODEs and DAEs interfaces were used to add a constraint so that the temperature at the probe was a specified value, either 25.5 or 29.4 °C for the 532 or 473 nm laser, respectively. The constraint is written as

$$T_{\mathrm{TC}} - T_{\mathrm{target}} = 0 \tag{14}$$

where T_{TC} is the temperature of the probe (i.e., thermocouple) and T_{target} is the target temperature (25.5 or 29.4 °C). The unknown $u(t)$ to be solved for is the temperature at either boundary, T_{source}, which is varied so that the condition described by Equation 14 is true. When heating comes from the laser, T_{source} is the temperature at the electrode-electrolyte interface. When heating comes from the Cu wire of the electrode lead, T_{source} is the temperature at the furthermost boundary of the Cu. Thus, T_{source} and the global equation are written as follows:

$$u(t) = T_{\mathrm{source}}(t) \tag{15}$$

$$f(u,t) = T_{\mathrm{TC}}(u,t) - T_{\mathrm{target}} = 0 \tag{16}$$

For the simulations of the chopped illumination experiments, a boundary heat source condition (Equation 17) was added in the electrode-electrolyte interface, to represent the heat generated by the laser,

$$-\mathbf{n} \cdot \mathbf{q} = Q_{\mathrm{b}} \tag{17}$$

where $\mathbf{n}$ is the normal vector and $\mathbf{q}$ is the heat flux. The magnitude of the heat source, Q_{b}, was described as a square wave with a period of 2 or 10 min, representing the chopping period. Thus, the value of Q_{b} oscillated from 0 to 2.38 W cm^{-2} periodically. Additionally, unlike the previous simulations, the heat and mass transfer were not assumed to be stationary, since the heat and mass transfer conditions are transient due to the intermittent heating. In that case, Equations 5 and 6 become Equations 18 and 19.

$$\frac{\partial \rho}{\partial t} + \nabla \cdot (\rho \mathbf{u}) = 0 \tag{18}$$

$$\rho \frac{\partial \mathbf{u}}{\partial t} + \rho(\mathbf{u} \cdot \nabla)\mathbf{u} = \nabla \cdot \left[-pI + \mu(\nabla \mathbf{u} + (\nabla \mathbf{u})^{\mathrm{T}}) - \frac{2}{3}\mu(\nabla \cdot \mathbf{u})I \right] + (\rho - \rho_{\mathrm{ref}})\mathbf{g} \tag{19}$$

Finally, the heat balance shown in Equation 7 becomes:

$$\rho C_p \left(\frac{\partial T}{\partial t} + \mathbf{u} \cdot \nabla T \right) + \nabla \cdot \mathbf{q} = Q_p + Q_{\mathrm{vd}} + Q \tag{20}$$

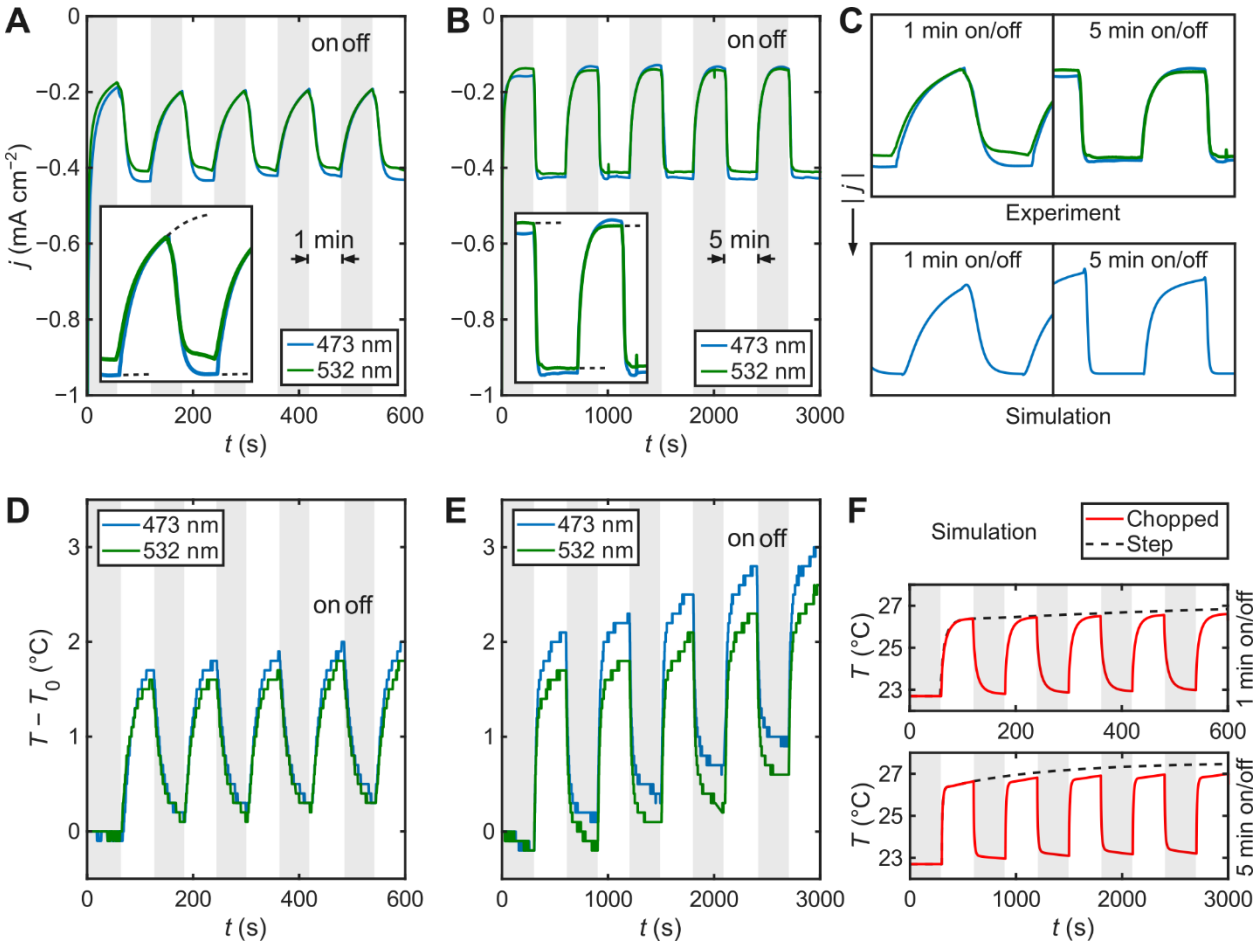

Figure S8. Experimental and simulated current density and temperature response during chopped illumination chronoamperometry. Experimental chronoamperograms when chopping 473 or 532 nm illumination at a period of (A) 2 min and (B) 10 min. Inset shows hysteretic current profile between light "on" and "off" states. (C) Comparison between experimental chronoamperograms acquired under chopped illumination and simulated chronoamperograms with an intermittent heat source at the electrode-electrolyte interface. (D, E) Temperature response measured by the thermocouple inserted in the electrode assembly during chopped illumination experiments at two different chopping periods. (F) Simulated temperature response at the thermocouple position from a heat source at the electrode-electrolyte interface applied intermittently (solid red lines) and in a single step (dashed lines).

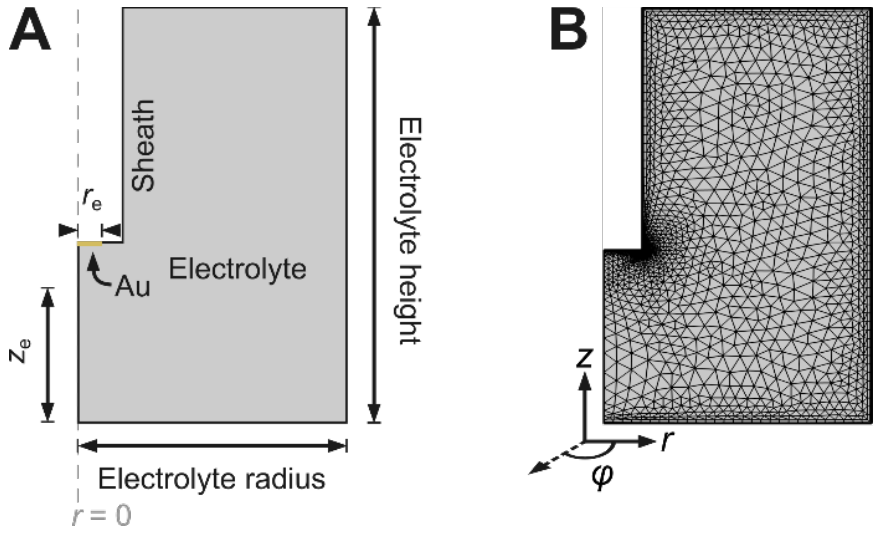

Figure S9. (A) 2D axisymmetric geometry and (B) computed finite-element mesh used in the mass transfer simulation. A 3D model is created by fully revolving the plane about the *r* axis.

Table S3. Geometrical parameters for simulation of electrochemical system.

Feature	Value	Unit
Electrode surface radius (r_e)	1	mm
Electrode assembly radius (r_a)	2	mm
Electrolyte (cell) radius	14	mm
Electrolyte height	24	mm
Electrode distance from bottom of cell (z_e)	8	mm

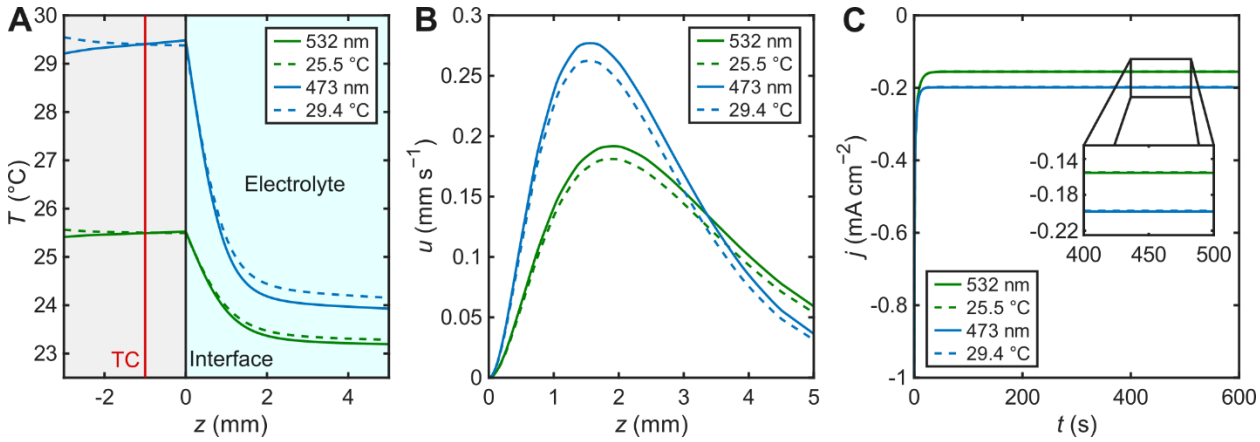

Figure S10. Finite-element simulations of different heat flux directions. The solid lines represent heat originating from the electrode surface, i.e., when a laser is used. The dashed lines represent heat originating from the resistive heater. In both cases, the temperature at the thermocouple (1 mm above the electrode surface) is the experimentally measured temperature (25.5 or 29.4 °C). (A) Axial temperature distribution along the working electrode. The red vertical line represents the position of the thermocouple. The black vertical line represents the electrode surface (z = 0). (B) Fluid velocity distribution away from the electrode surface. (C) Simulated chronoamperograms showing the difference in current density when the heat source is at the electrode-electrolyte interface (solid lines) or the Cu wire of the electrode lead (dashed lines) in the electrode assembly.

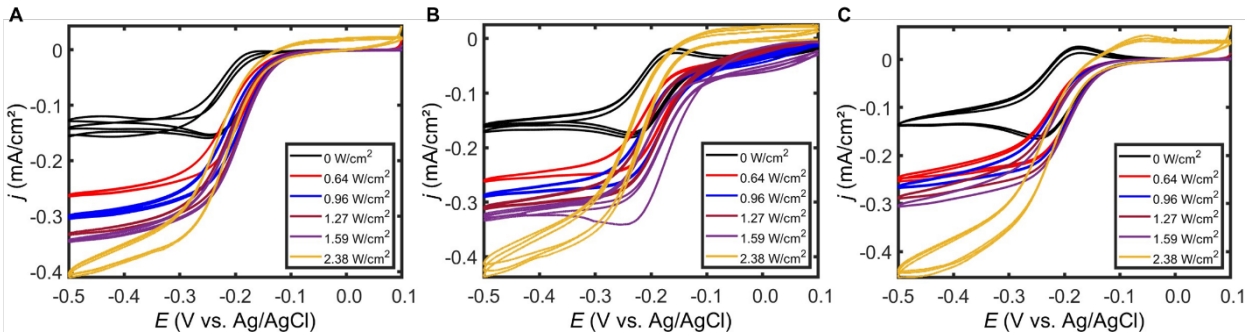

Figure S11. Cyclic voltammograms of 5 mM $[Ru(NH_3)_6]^{3+}$ at roughened Au at 1 mV s^{-1} under dark (black curves) and light (colored curves) conditions at different 532 nm incident intensities. Panels represent independent trials.

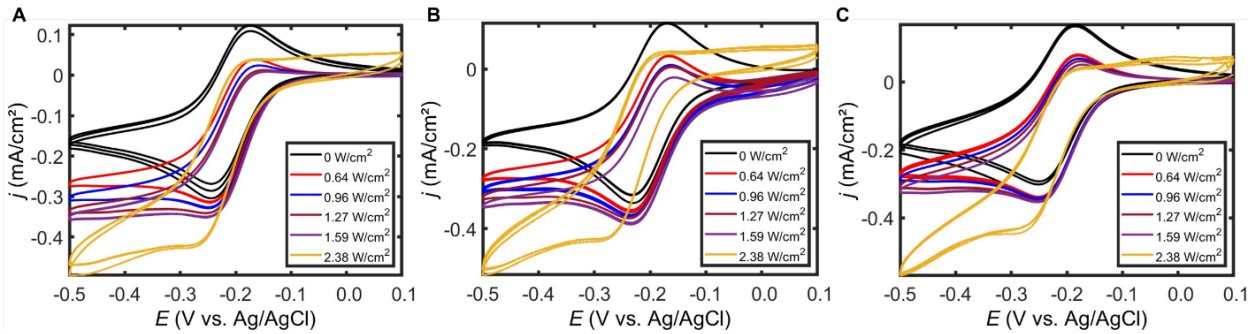

Figure S12. Cyclic voltammograms of 5 mM $[Ru(NH_3)_6]^{3+}$ at roughened Au at 5 mV s^{-1} under dark (black curves) and light (colored curves) conditions at different 532 nm incident intensities. Panels represent independent trials.

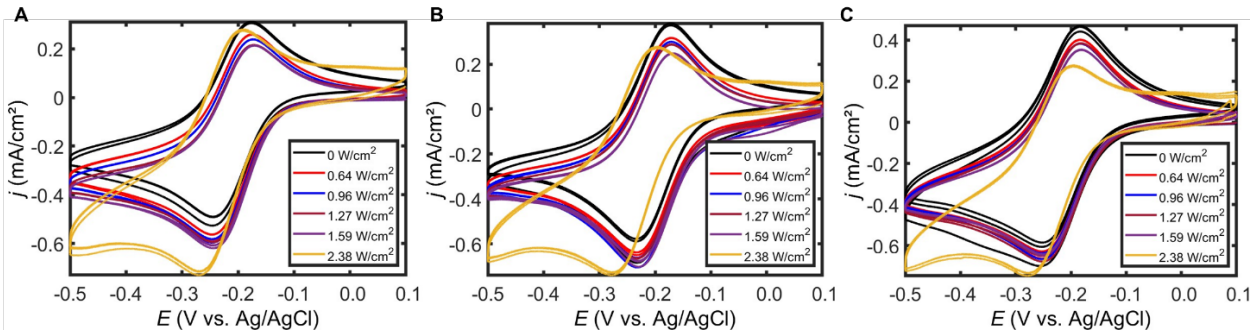

Figure S13. Cyclic voltammograms of 5 mM $[Ru(NH_3)_6]^{3+}$ at roughened Au at 20 mV s^{-1} under dark (black curves) and light (colored curves) conditions at different 532 nm incident intensities. Panels represent independent trials.

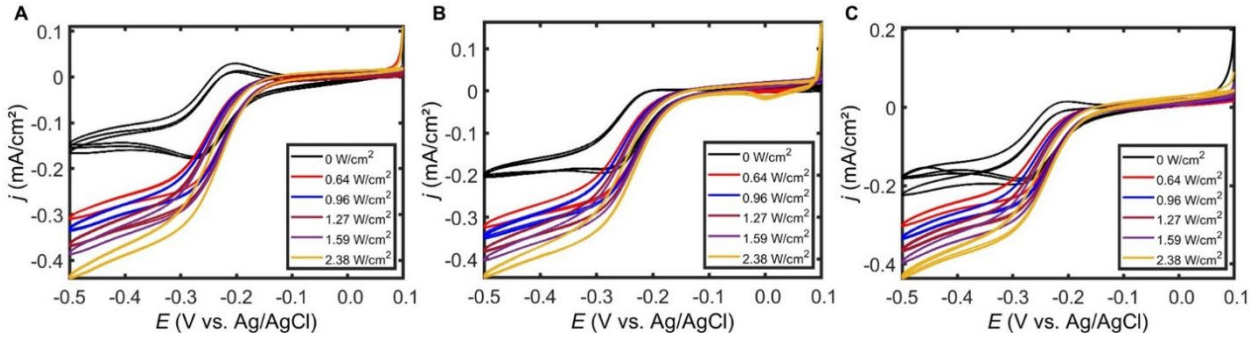

Figure S14. Cyclic voltammograms of 5 mM $[Ru(NH_3)_6]^{3+}$ at roughened Au at 1 mV s^{-1} under dark (black curves) and light (colored curves) conditions at different 473 nm incident intensities. Panels represent independent trials.

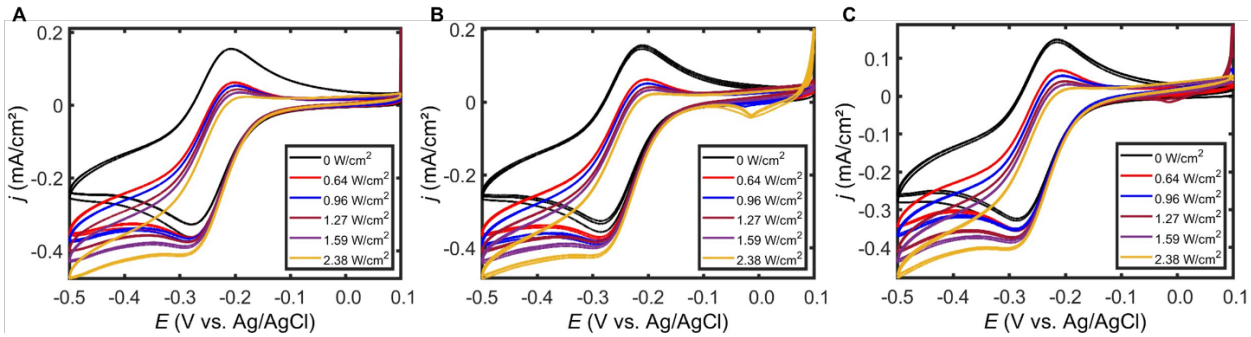

Figure S15. Cyclic voltammograms of 5 mM $[Ru(NH_3)_6]^{3+}$ at roughened Au at 5 mV s^{-1} under dark (black curves) and light (colored curves) conditions at different 473 nm incident intensities. Panels represent independent trials.

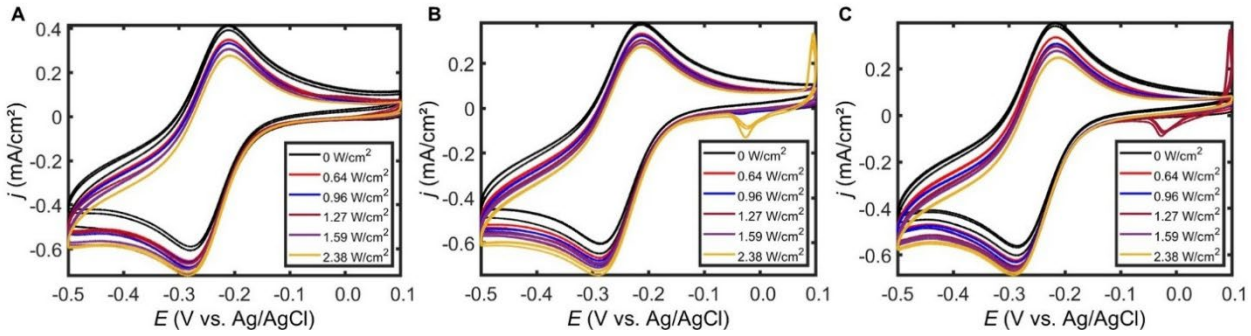

Figure S16. Cyclic voltammograms of 5 mM $[Ru(NH_3)_6]^{3+}$ at roughened Au at 20 mV s^{-1} under dark (black curves) and light (colored curves) conditions at different 473 nm incident intensities. Panels represent independent trials.

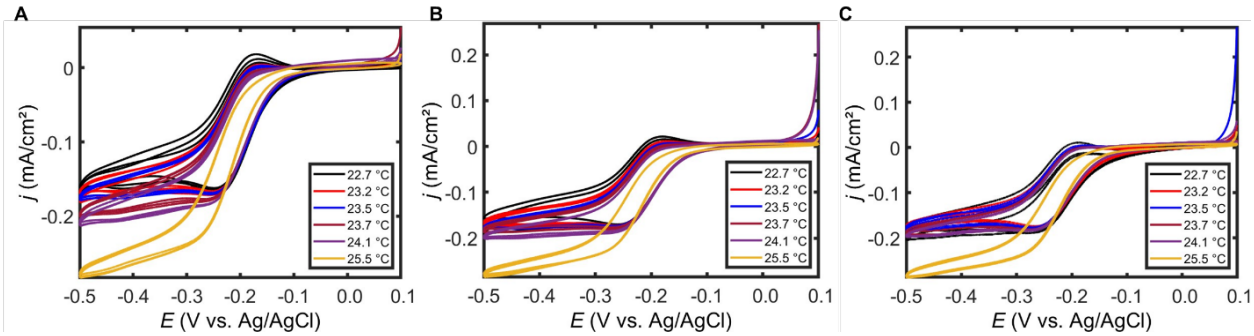

Figure S17. Cyclic voltammograms of 5 mM $[Ru(NH_3)_6]^{3+}$ at roughened Au at 1 mV s^{-1} under dark (black curves) and heated electrode (colored curves) conditions at different electrode surface temperatures, which correspond to the measured surface temperature when under 0.64, 0.96, 1.27, 1.54, or 2.38 W cm^{-2} illumination at 532 nm, respectively. Panels represent independent trials.

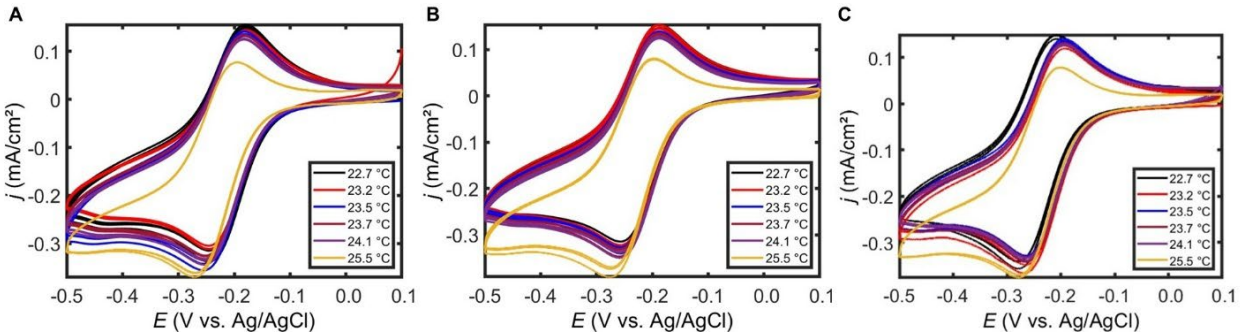

Figure S18. Cyclic voltammograms of 5 mM $[Ru(NH_3)_6]^{3+}$ at roughened Au at 5 mV s^{-1} under dark (black curves) and heated electrode (colored curves) conditions at different electrode surface temperatures, which correspond to the measured surface temperature when under 0.64, 0.96, 1.27, 1.54 or 2.38 W cm^{-2} illumination at 532 nm, respectively. Panels represent independent trials.

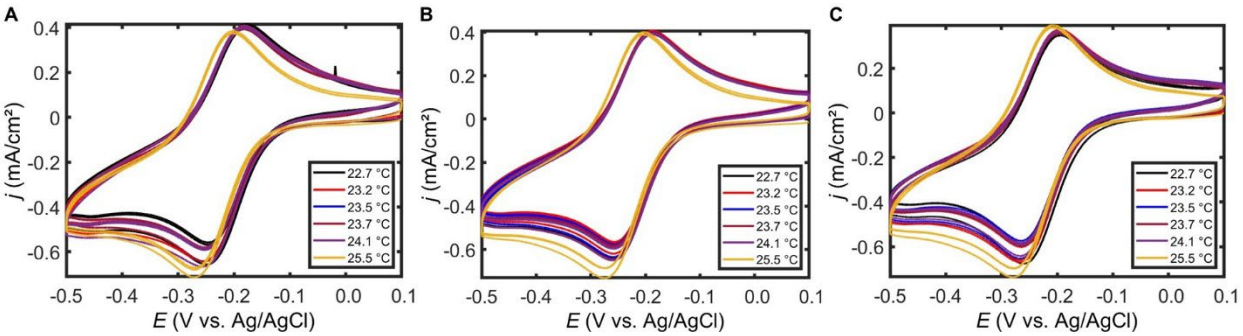

Figure S19. Cyclic voltammograms of 5 mM $[Ru(NH_3)_6]^{3+}$ at roughened Au at 20 mV s^{-1} under dark (black curves) and heated electrode (colored curves) conditions at different electrode surface temperatures, which correspond to the measured surface temperature when under 0.64, 0.96, 1.27, 1.54 or 2.38 W cm^{-2} illumination at 532 nm, respectively. Panels represent independent trials.

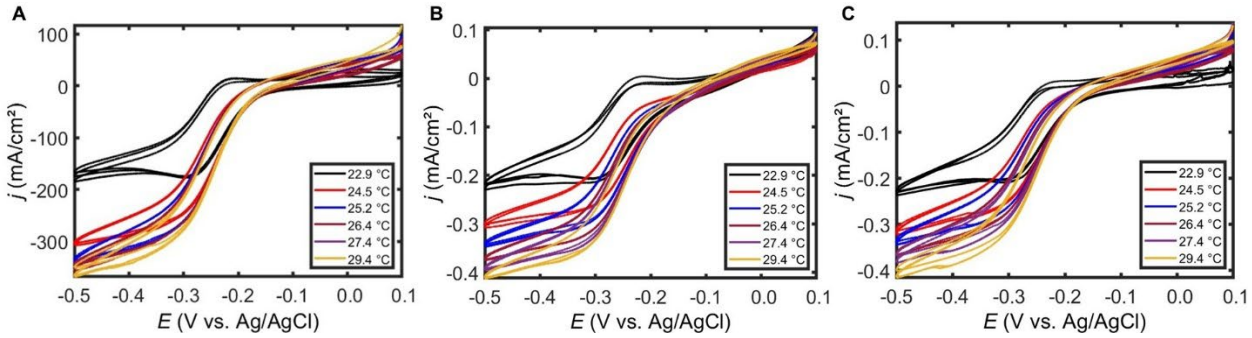

Figure S20. Cyclic voltammograms of 5 mM $[Ru(NH_3)_6]^{3+}$ at roughened Au at 1 mV s^{-1} under dark (black curves) and heated electrode (colored curves) conditions at different electrode surface temperatures, which correspond to the measured surface temperature when under 0.64, 0.96, 1.27, 1.54 or 2.38 W cm^{-2} illumination at 473 nm, respectively. Panels represent independent trials.

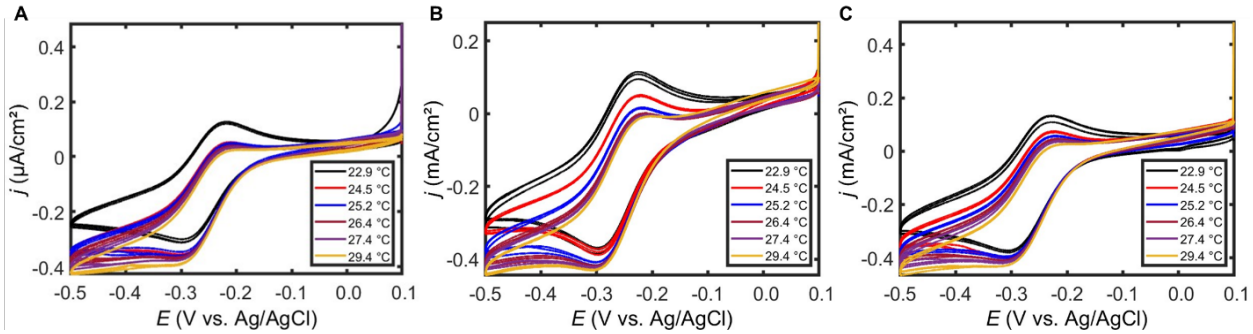

Figure S21. Cyclic voltammograms of 5 mM $[Ru(NH_3)_6]^{3+}$ at roughened Au at 5 mV s^{-1} under dark (black curves) and heated electrode (colored curves) conditions at different electrode surface temperatures, which correspond to the measured surface temperature when under 0.64, 0.96, 1.27, 1.54 or 2.38 W cm^{-2} illumination at 473 nm, respectively. Panels represent independent trials.

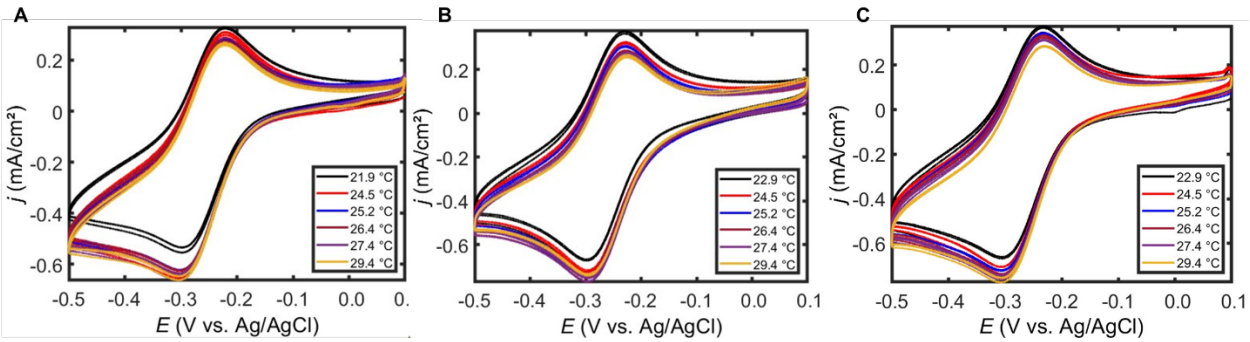

Figure S22. Cyclic voltammograms of 5 mM $[Ru(NH_3)_6]^{3+}$ at roughened Au at 20 mV s^{-1} under dark (black curves) and heated electrode (colored curves) conditions at different electrode surface temperatures, which correspond to the measured surface temperature when under 0.64, 0.96, 1.27, 1.54 or 2.38 W cm^{-2} illumination at 473 nm, respectively. Panels represent independent trials.

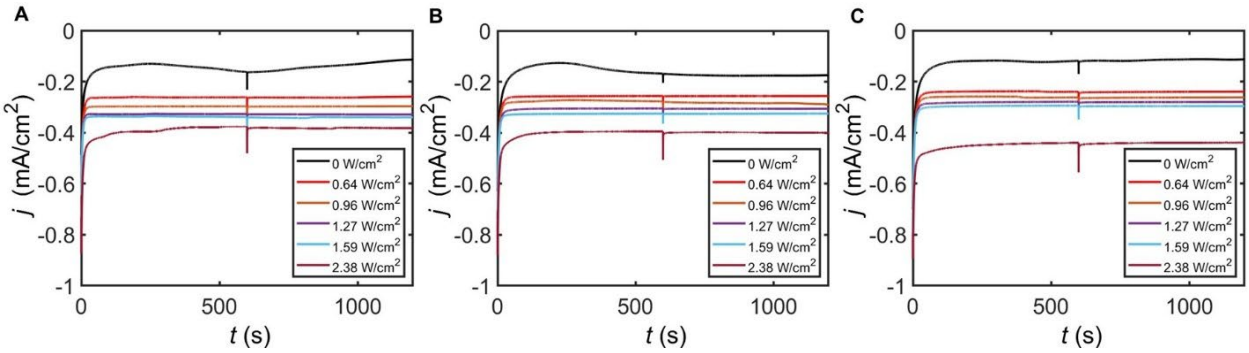

Figure S23. Chronoamperograms of 5 mM $[Ru(NH_3)_6]^{3+}$ at roughened Au at −0.45 V vs. Ag/AgCl (3 M KCl) under dark (black curves) and illuminated (colored curves) conditions at different incident intensities at 532 nm. Panels represent independent trials. Data shown is two consecutive chronoamperograms, the second beginning at t = 600 s.

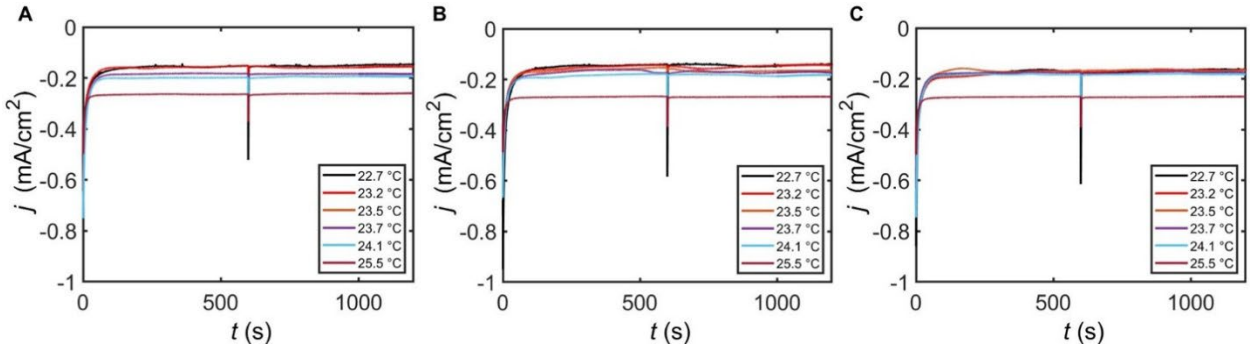

Figure S24. Chronoamperograms of 5 mM $[Ru(NH_3)_6]^{3+}$ at roughened Au at −0.45 V vs. Ag/AgCl (3 M KCl) under dark (black curves) and heated electrode (colored curves) conditions at different electrode surface temperatures, which correspond to the measured surface temperature when under 0.64, 0.96, 1.27, 1.54 or 2.38 W cm^{-2} illumination at 532 nm, respectively. Panels represent independent trials. Data shown is two consecutive chronoamperograms, the second beginning at t = 600 s.

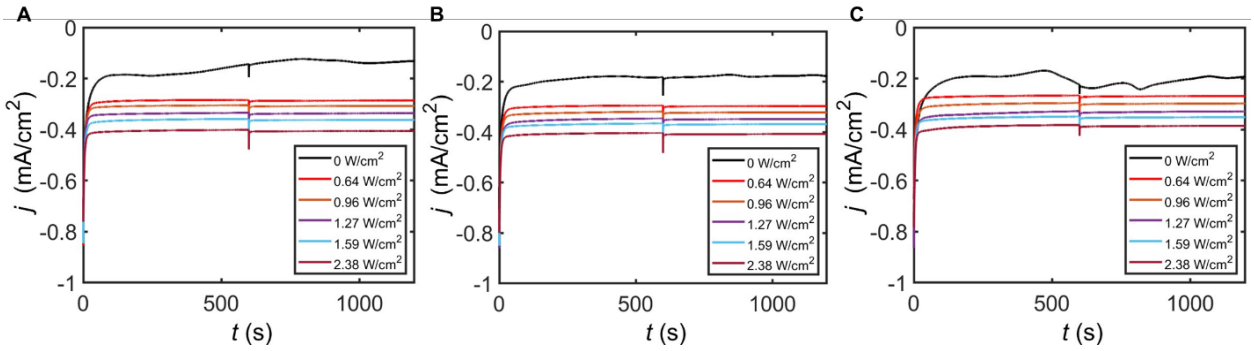

Figure S25. Chronoamperograms of 5 mM $[Ru(NH_3)_6]^{3+}$ at roughened Au at −0.45 V vs. Ag/AgCl (3 M KCl) under dark (black curves) and illuminated (colored curves) conditions at different incident intensities at 473 nm. Panels represent independent trials. Data shown is two consecutive chronoamperograms, the second beginning at t = 600 s.

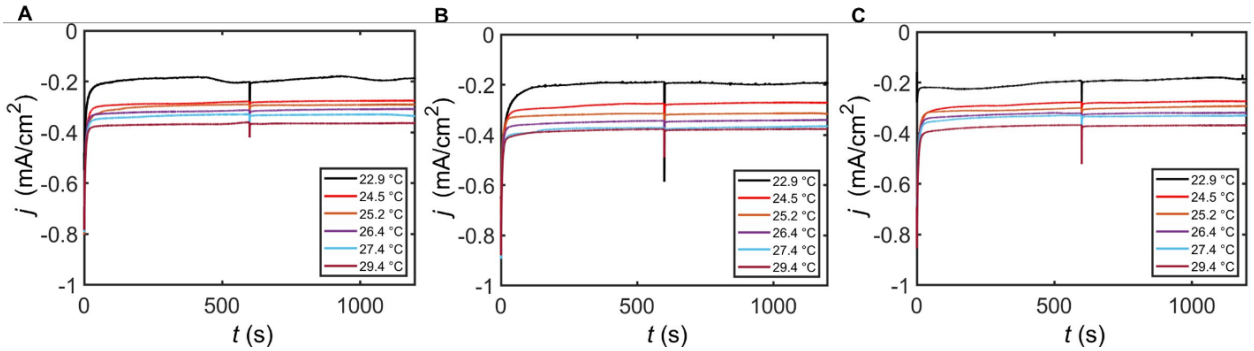

Figure S26. Chronoamperograms of 5 mM $[Ru(NH_3)_6]^{3+}$ at roughened Au at −0.45 V vs. Ag/AgCl (3 M KCl) under dark (black curves) and heated electrode (colored curves) conditions at different electrode surface temperatures, which correspond to the measured surface temperature when under 0.64, 0.96, 1.27, 1.54 or 2.38 W cm^{-2} illumination at 473 nm, respectively. Panels represent independent trials. Data shown is two consecutive chronoamperograms, the second beginning at t = 600 s.

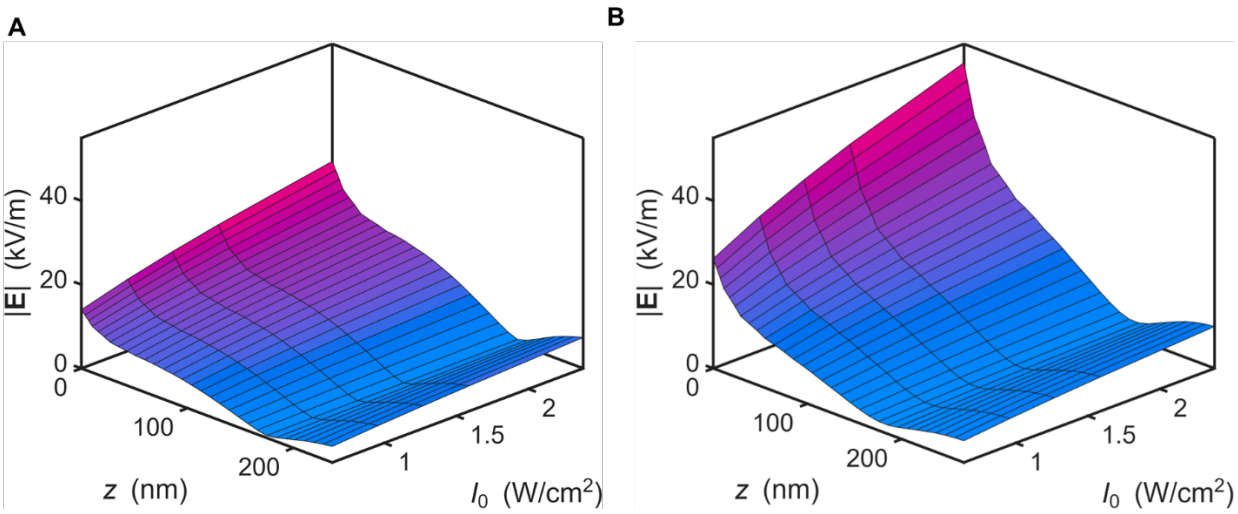

Figure S27. Simulated magnitude of the electric field gradient away from the nanoparticle surface under (A) 473 nm or (B) 532 nm circularly polarized light excitation.

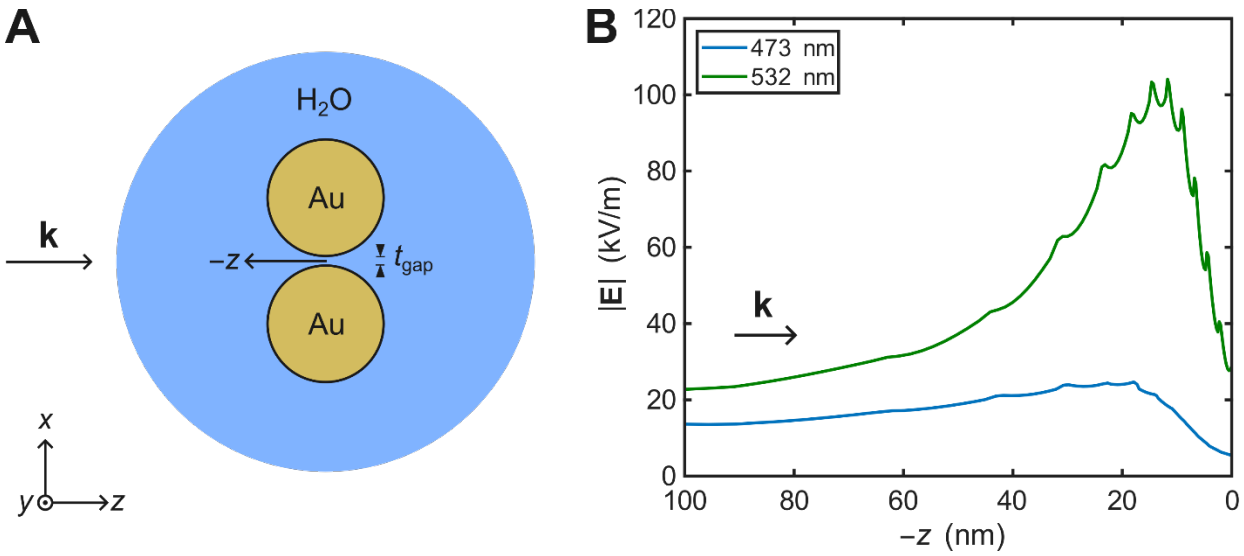

Figure S28. Simulated magnitude of the electric field gradient near a dimer of Au nanospheres with a 1 nm gap under 2.38 W cm^{-2} circularly polarized illumination at 473 and 532 nm.

References

S1 Md. Al-Amin, J. V. Hemmer, P. B. Joshi, K. Fogelman and A. J. Wilson, *Commun Chem*, 2024, **7**, 70.

S2 Md. Al-Amin, J. V. Hemmer and A. J. Wilson, *ACS Appl. Mater. Interfaces*, 2025, acsami.5c12578.

S3 A. D. Rakić, A. B. Djurišić, J. M. Elazar and M. L. Majewski, *Appl. Opt.*, 1998, **37**, 5271.

S4 M. Daimon and A. Masumura, *Appl. Opt.*, 2007, **46**, 3811.